International Journal of Minerals, Metallurgy and Materials
https://doi.org/10.1007/s12613-020-2072-6

In vitro bioactivity and corrosion of PLGA/hardystonite composite-coated magnesium-based nanocomposite for implant applications

Mahmood Razzaghi, *Masoud Kasiri-Asgarani*, *Hamid Reza Bakhsheshi-Rad*, *and Hamid Ghayour*

Advanced Materials Research Center, Department of Materials Engineering, Najafabad Branch, Islamic Azad University, Najafabad, Iran
(Received: 15 December 2019; revised: 27 March 2020; accepted: 13 April 2020)

Abstract: A type of polymer/ceramic coating was introduced on a magnesium-based nanocomposite, and the nanocomposite was evaluated for implant applications. The microstructure, corrosion, and bioactivity of the coated and uncoated samples were assessed. Mechanical alloying followed by sintering was applied to fabricate the Mg–3Zn–0.5Ag–15NiTi nanocomposite substrate. Moreover, different contents of poly(lactic-co-glycolic acid) (PLGA) coatings were studied, and 10wt% of PLGA content was selected. The scanning electron microscopy (SEM) images of the bulk nanocomposite showed an acceptable homogenous dispersion of the NiTi nanoparticles (NPs) in the Mg-based matrix. In the *in vitro* bioactivity evaluation, following the immersion of the uncoated and coated samples in a simulated body fluid (SBF) solution, the Ca/P atomic ratio demonstrated that the apatite formation amount on the coated sample was greater than that on the uncoated nanocomposite. Furthermore, assessing the corrosion resistance indicated that the coatings on the Mg-based substrate led to a corrosion current density (i_{corr}) that was considerably lower than that of the substrate. Such a condition revealed that the coating would provide an obstacle for the corrosion. Based on this study, the PLGA/hardystonite (HT) composite-coated Mg–3Zn–0.5Ag–15NiTi nanocomposite may be suitably applied as an orthopedic implant biomaterial.

Keywords: magnesium; nanocomposite; corrosion; biocompatibility; poly(lactic-co-glycolic acid); hardystonite

1. Introduction

Over the last years, researchers have been increasingly interested in biodegradable Mg alloys as significant alternative materials for implants. This is because Mg alloys offer potential solutions to today's common issues of the biomaterials used for orthopedic applications, such as the stress shielding concerns related to conventional metallic implants and the inferior mechanical properties of the polymeric biomaterials [1–2]. Magnesium is widely accepted to be biodegradable, biocompatible, and osteoconductive [3]. Moreover, research has shown that the human body can efficiently metabolize Mg degradation products, thus preventing the requirement of a second surgery for implant elimination after tissue repair [4]. Nevertheless, multiple concerns should be considered before considering pure Mg for tissue engineering, which include the low corrosion resistance and high degradation rate. This article explores Zn and Ag for reinforcing Mg to promote its mechanical properties, corrosion resistance, and antibacterial activities in order to satisfy clinical necessities [5–7]. Zinc contributes vitally to the human body, as it is essential for multiple biological activities [8]. Researchers have demonstrated poor antibacterial capabilities of the Mg-based composites: they result in infected implants as well as postoperative issues; notably, a bone infection is one of the crucially destructive problems of using these composites, which can lead to severe economic and clinical complications [9]. As one of the alternative approaches, silver antimicrobial agents have been utilized to reduce bacterial adhesion and suppress the bio-film progression. Some studies have shown extreme antimicrobial activities of silver against gram-negative and gram-positive bacteria, protozoa, fungi, and specific viruses, as well as the antibiotic-resistant strains of these microorganisms [10].

One way to improve the mechanical properties of Mg is the use of appropriate alloying elements such as zinc, aluminum, calcium, and silver [11]. According to previous studies [12–13], strength is reinforced due to the solid solution and precipitation reinforcement via Zn utilization at lower contents. Du *et al.* [14] showed that the tensile strength and

Corresponding authors: Masoud Kasiri-Asgarani E-mail: m.kasiri.a@gmail.com, m.kasiri@pmt.iaun.ac.ir;
Hamid Reza Bakhsheshi-Rad E-mail: rezabakhsheshi@gmail.com, rezabakhsheshi@pmt.iaun.ac.ir

formability of Mg can be improved through grain refinement by incorporating Zn alloying element. Other studies have also suggested possible enhancement of the mechanical properties of Mg alloys by adding a trace amount of Ag [15–17]. Zhang *et al.* [18] showed that after Ag was incorporated into Mg–Nd–Zn–Zr alloys, their grain size decreased and the second-phase particles volume increased. Another research [19] showed that the mechanical properties of Mg–2.4Zn alloy can be improved by incorporating Ag. Magnesium-matrix composites have been fabricated to improve the characteristics of Mg [20]. Composite strengthening is well known to be a practical method for enhancing the mechanical properties of Mg alloys [21]. Wakeel *et al.* [22] proved that the mechanical properties of Mg can be improved by strengthening the matrix using NiTi nanoparticles (NPs).

Using composite materials has been also approved as one of the options for achieving the increased corrosion resistance and antibacterial activities desirable for medical applications [23]. Although ceramic reinforcements such as SiC, B_4C, TiC, Y_2O_3, TiB_2, and Al_2O_3 possibly enhance the strength of Mg-based matrixes, the formability of the fabricated composite would be reduced because of the generation of brittle phases in the matrix-reinforcement interface areas. However, the problem of formability can be solved by using metallic reinforcements such as Cu, Ni, and Ti [24]. Another study [25] has shown that the NiTi alloy as one of the metallic reinforcements would have reasonable mechanical properties and biocompatibility; therefore, it would be suitable for use in medical applications. Esen [26] reinforced Mg with 5vol%, 10vol%, and 15vol% of micron-sized NiTi and found that the mechanical properties of Mg were enhanced by NiTi through grain refinement and the NiTi incorporation to form a composite. The results also demonstrated that the composite composed of 5vol% (16.4wt%) of NiTi had the most acceptable outputs, while the composites with 10vol% and 15vol% NiTi featured reduced mechanical properties. Wakeel *et al.* [22] applied the sintering fabrication process and reinforced Mg with 2wt% NiTi NPs. They found that the microhardness and compressive strength of the composite were 30% greater than those of the Mg matrix. Thus, a powder-metallurgy fabrication method such as mechanical alloying can be concluded to be a feasible method for fabricating Mg-based composites. Some studies have revealed that the mechanical characteristics of the Mg-based biocomposites can be enhanced by mechanical alloying by modifying the grain size and homogenous dispersion of reinforcement particles [27–29].

Nevertheless, other studies have illustrated that biodegradable Mg would have low corrosion resistance, causing quick degradation, the formation of great volumes of H_2 gas, and an increase in the pH of the surrounding tissue [30]. Therefore, researchers have employed alloying and surface modification to reduce the Mg degradation rate and enhance the potential biomedical applications [31–33]. Based on the results of the studies, alloying would merely be suitable for preventing general corrosion; it cannot prevent the galvanic degradation of Mg-based implants in the initial phases of the implant presence in the body; this degradation is generated by the second-phase particles and could result in the evolution of non-smooth corrosion [34]. Therefore, surface modifications through polymer and other inorganic/organic coatings have been applied for reducing the corrosion rate of Mg alloys, preserving the mechanical properties, and accelerating the tissue healing procedure [35]. The present article describes a new type of coating on Mg-based implants, whereby the coated part has superior corrosion resistance compared with the uncoated part. Poly(lactic-co-glycolic acid) (PLGA) has been chosen because of its bioresorbability and cytocompatibility, which are necessary for tissue engineering applications. In addition, hardystonite (HT), which is one of the calcium zinc silicate ceramics, was incorporated into the PLGA polymer. It exhibited excellent bioactivity because of the release of the ions such as Ca, Si, and Zn into the biological environment, which helps the formation of apatite on the implant surface.

2. Experimental

2.1. Fabrication process

The fabrication process of the research samples and the evaluations are described in Fig. 1. This procedure began by mixing pure Mg powder (50 μm average particle size, 99.8% purity), Zn powder (7.5 μm average particle size, 98.8% purity), and Ag powder (6.5 μm average particle size, 99.9% purity), all purchased from Sigma-Aldrich Co., USA, with nano-sized NiTi powder (20–150 nm particle size). Table 1 presents the nanocomposite composition. The mechanical alloying of the mixed powder was then conducted by mixing the powder in a planetary ball mill for 25 h at ambient temperature. The mixed powder had been charged into an argon atmosphere-controlled ball mill steel vial with a limit of less than 4 mg/m^3 oxygen content. For milling, 20 mm-diameter stainless steel balls were utilized, and the allowable number of balls in the vial was computed based on the ball-to-powder weight ratio of 15:1. The mechanical alloying parameters in the nanocomposites milling are presented in Table 2 [36–37].

The milled powder was compacted under 400 MPa pressure. In the next step, the green compacted sample was sintered. The sintering process comprised two continuous stages: 2 h at 200°C and 2 h at 530°C, with a 5°C/min heating rate in an argon atmosphere-controlled furnace. The total porosity (φ_{total}) of the sintered nanocomposite was computed based on the relation $\varphi_{total} = \left(1 - \frac{\rho_{bulk}}{\rho_{composite}}\right) \times 100\%$. The nanocomposite theoretical density ($\rho_{composite}$) was computed

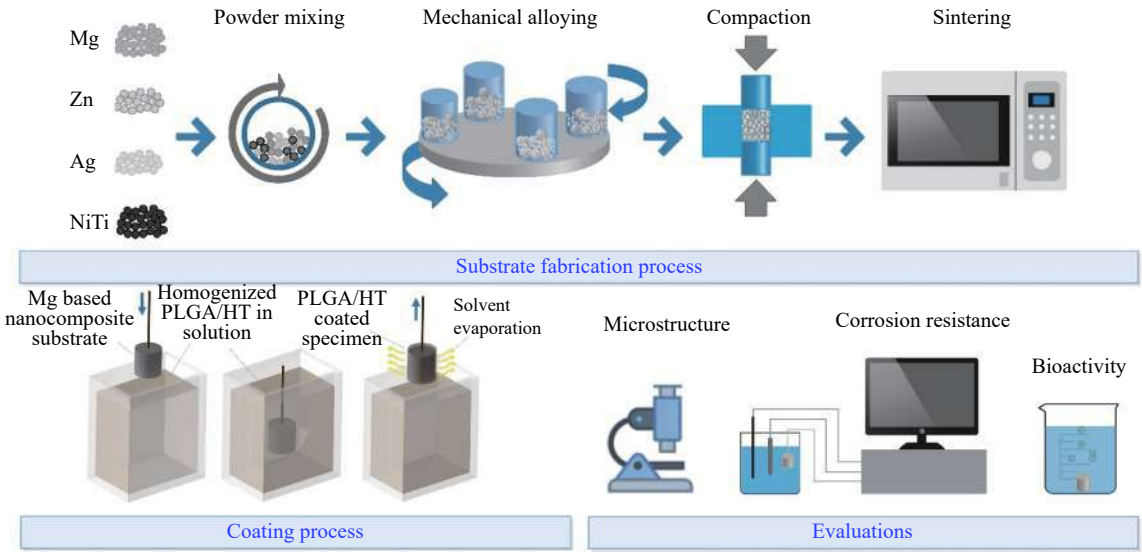

Fig. 1. Schematic illustration of the fabrication process and evaluations of the research.

Table 1. Composition and theoretical density of the nanocomposite sample

Composition / wt%				Theoretical density / ($g \cdot cm^{-3}$)
Mg	Zn	Ag	NiTi	
82.025	2.550	0.425	15.000	1.998

Table 2. Parameters of the mechanical alloying process adopted for milling the powders

Rotation speed / ($r \cdot min^{-1}$)	300
Ball-to-powder weight ratio	15:1
Vial and ball material	Steel
Mass of powder / g	30
Milling time / h	25
Capacity of the vial / mL	250
Diameter of the balls / mm	20

based on the powder ingredients through the following equation:

$$\rho_{composite} = f_{Mg} \cdot \rho_{Mg} + f_{Zn} \cdot \rho_{Zn} + f_{Ag} \cdot \rho_{Ag} + f_{NiTi} \cdot \rho_{NiTi} \quad (1)$$

where f_{Mg}, f_{Zn}, f_{Ag}, and f_{NiTi} are volume fractions of Mg, Zn, Ag and NiTi, respectively; ρ_{Mg}, ρ_{Zn}, ρ_{Ag}, and ρ_{NiTi} are densities of Mg, Zn, Ag and NiTi, respectively. To measure the bulk density (ρ_{bulk}), the mass of the sample was divided by its volume. The mass of the specimen was measured using a digital balance, and its volume was computed based on the specimen dimensions. Then, the calculated bulk density was validated by this relation [38]: $\rho_{bulk} = \frac{W_d}{W_w - W_s}$; W_d, W_s, and W_w are the sample weights in dry and water-soaked conditions and after soaking in water, respectively. Afterward, the total porosity, consisting of the interconnected pore network, was computed.

For the dip-coating procedure, to obtain the suspension, 10 mg PLGA (an average molecular weight of 50000 and D,L-lactide : glycolide molar ratio of 50:50, Evonik, Germany) was initially dissolved in 100 mg (75.2 mL) dichloromethane (CH_2Cl_2) and shaken at 400 r/min for 2 h so that a jelly-like material was generated. Finally, 1 mg HT was slowly added to the solution, and the mixture was shaken for 30 min. The suspension was then ready for the dip-coating procedure. The specimen was polished using 1200 grit SiC polishing paper, rinsed with distilled water, and dried. It was then immersed in the suspension for 10 s and subsequently dried for 5 min. This immersion–drying cycle was repeated five times.

2.2. Structural characterization

According to the research design, the structures of the uncoated bulk nanocomposite and PLGA- and PLGA/HT composite-coated specimens were characterized using scanning electron microscopy (SEM, Quanta 200). X-ray diffraction (XRD, Siemens/Bruker D5000) was employed to detect the phases, using Cu-K_α radiation (40 mA, 45 kV) with the angles of diffraction (2θ) range from 30° to 80° and a scanning rate of 4°/min. Fourier-transform infrared (FTIR) spectroscopy was utilized to detect the functional groups of the surface of the coated samples, recorded in the spectral range from 4000 to 400 cm^{-1}.

2.3. *In vitro* bioactivity

To examine the bioactivity behavior, all bare and coated samples were immersed into a cup containing a simulated body fluid (SBF) solution of 100 mL under (36.5 ± 1)°C for 7 d. Afterward, the specimens were rinsed with distilled water and then dried in ambient condition.

2.4. *In vitro* degradation and corrosion

The electrochemical studies of the bare and coated specimens were performed using a potentiostat/galvanostat (Princeton Applied Research PARSTAT 2273). The 0.8 cm^2-sur-

face-area specimens were immersed in a three-electrode cell composing of Kokubo solution at 37°C with pH of 7.4 [39]. Moreover, the working electrode in the cell was applied with a saturated calomel electrode and platinum wire as the reference and counter electrodes, respectively. The potential range of potentiodynamic polarization was from −250 to 1300 mV against the open-circuit potential, and the scan rate was 1 mV/s.

2.5. *In vitro* cytotoxicity

The MTT (3-(4,5-dimethylthiazol-2-yl)-2,5-diphenyltetrazolium-bromide) assay was utilized to evaluate the *in vitro* cytotoxicity of the substrate nanocomposite. The indirect MTT (Sigma, Saint Louis, USA) assay was used based on the extraction method. The details of the test method can be found in Ref. [40].

2.6. Statistical analysis

Here, data are expressed as mean ± standard deviation, and statistical analyzes were performed using two-tailed t-tests with Sigmaplot software if needed. The statistical significance is indicated by probability (P) as follows: *P-value < 0.05; **P-value < 0.01; ***P-value < 0.001.

3. Results and discussion

3.1. Microstructural characterization

The SEM micrograph and energy-dispersive X-ray spectroscopy (EDS) maps of the Mg–3Zn–0.5Ag–15NiTi nanocomposite substrate after the sintering process are displayed in Fig. 2(a). As can be seen, the NiTi NP distribution in the matrix was acceptably uniform with minimum clustering. This can be attributed to the optimum processing parameters and the effect of Ar disintegration on the mechanical alloying process. A reasonably long mechanical alloying process can completely blend the nanocomposite ingredients to form a uniform nanocomposite. The XRD patterns of the nanocomposite before and after milling and sintering are presented in Fig. 2(b). As can be seen, the intensity of the peaks after sintering increased. This could be due to the increase in the grain size of the nanocomposite resulting from heat treatment in the sintering process. The $Mg_{51}Zn_{20}$ intermetallic phase was detected in the substrate after milling and sintering.

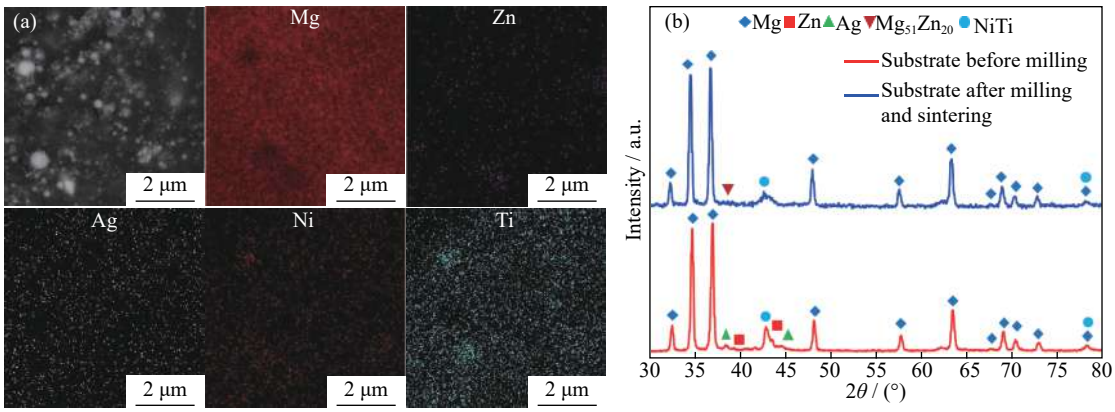

Fig. 2. (a) SEM image and the corresponding EDS maps of the Mg–3Zn–0.5Ag–15NiTi nanocomposite substrate after sintering; (b) XRD patterns of the substrate nanocomposites before milling and after sintering.

Fig. 3 shows the SEM micrographs of the surface and cross section of the 10wt% PLGA/HT composite-coated sample. As can be seen, the coating had a uniform structure with little changes in thickness. The average thickness of the coated layer was measured as about 18 μm. Fig. 4 indicates that the FTIR spectrum of the coated specimens comprised C–O, C=O, and C–H bands, related to PLGA, and Si–O–Si, Si–O, and Zn–O bands, related to HT. The characteristic group contributions consistent with PLGA structure contained C–O groups in the wavenumber range of 1250–1110 cm^{-1}, C=O band at about 1610 cm^{-1}, and $–(CH_2)_4–$ skeletal groups in the wavenumber ranges of 2980–2810 cm^{-1} and 1460–1230 cm^{-1}. The absorption of the C=O bond represents the existence of an aliphatic ester of PLGA on the surface. The formation of HT and PLGA was confirmed based on the FTIR spectroscopy.

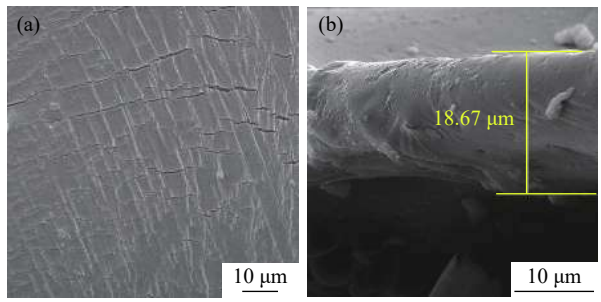

Fig. 3. SEM micrographs of the (a) surface and (b) cross section of the 10wt% PLGA/HT composite-coated sample.

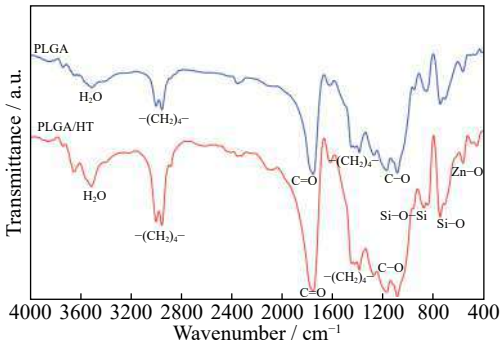

Fig. 4. FTIR absorption spectra of the 10wt% PLGA- and PLGA/HT composite-coated specimens.

Fig. 5 displays the SEM image and relevant EDS maps of the coated area of the PLGA/HT composite-coated specimen. The EDS maps show the presence of C, O, Si, Ca, and Zn elements. The presence of C and O elements indicates the formation of a PLGA layer, and the existence of Si, Ca, and Zn signifies the HT incorporated into PLGA coating. The distributions of Si, Ca, and Zn in the EDS maps (Figs. 5(d)–5(f)) prove the uniform distribution of HT particles in PLGA. This can be attributed to homogenized PLGA/HT suspension achieved by the adequate stirring of the HT powder in the PLGA solution.

3.2. *In vitro* bioactivity

First, to select the PLGA content for coating, the coated samples with 2wt%, 6wt%, and 10wt% PLGA were compared with the uncoated nanocomposite. Fig. 6 shows the images of the uncoated and coated samples with 2wt%, 6wt%,

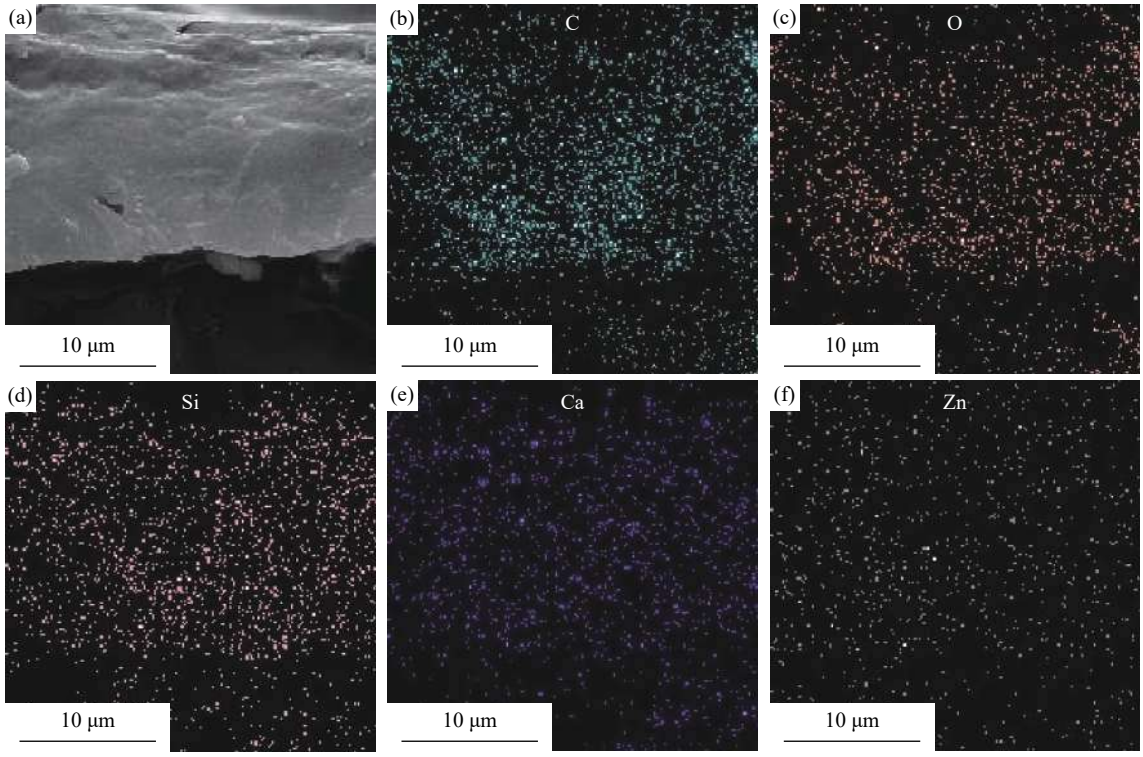

Fig. 5. (a) SEM image and (b)–(f) the corresponding EDS maps of the coated area of the PLGA/HT composite-coated specimen.

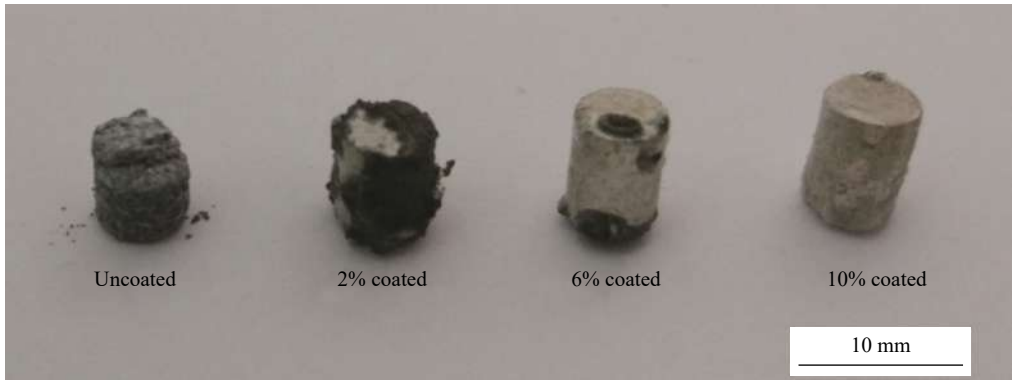

Fig. 6. Images of the uncoated and coated nanocomposites after SBF immersion.

and 10wt% PLGA after immersion in the Kokubo solution for 7 d. The sample corrosion rate decreased with increasing PLGA content.

Fig. 7 displays the EDS spectrum and corroded morphologies of the uncoated and 2wt%-, 6wt%-, and 10wt%-PLGA-coated samples after immersion in the Kokubo solution for 7 d. The apatite layers were shredded because of their highly porous nature. Degradation happened in the form of detached fine particles. Open holes, shredded layers, and cracks existed on the corroded surface because of the release of H_2 gas and Mg^{2+} ions. The apatite shredding and traces of the detached P and Ca particles may be readily determined as the holes/cracks. According to Fig. 7, the growth of the apatite layer formation is proved by the EDS analyses. With an increase in the PLGA content, the corrosion degrees of the samples reduced. Regarding the EDS outputs, the Ca/P atomic ratio was enhanced with an increase in the PLGA content. This may be due to the increased protection of denser coatings that would cause a more stable surface to form the apatite layer. Moreover, the EDS analyses revealed O and Mg as the key elements in the layer, which shows that $Mg(OH)_2$ was the key compound of the layer. However, Yang and Zhang [41] showed that the $Ca_3Mg_3(PO_4)_4$ phase was formed on the Mg alloy after immersion in SBF. Finally, 10wt% PLGA content was selected for the coating procedure.

For the next step of the coating, HT particles with the PLGA content of 10wt% was added to the coating, and the PLGA/HT composite-coated sample was prepared for evaluation. Figs. 8(a) and 8(b) show the SEM micrograph and EDS analysis of the 10wt% PLGA/HT composite-coated specimen after immersion in SBF. The results indicate that the apatite layer was better formed on the surface of this specimen, compared to the surface of the 10wt% PLGA-coated specimen; this could be due to the bioactivity effect of HT. The Ca/P atomic ratios related to the products of the 10wt% PLGA-coated and PLGA/HT-coated specimens were about 1.77 and 1.82, respectively, representing the formation of hydroxyapatite.

The XRD patterns of the uncoated and 10wt% PLGA/HT-coated samples after immersion in SBF for 14 d are shown in Fig. 8(c). The XRD pattern confirmed the presence of $Mg(OH)_2$ as the main corrosion product of the uncoated sample, and a trace amount of hydroxyapatite (HA) was also observed in this diffraction pattern. Strong peaks of $Mg(OH)_2$ indicated the occurrence of severe corrosion attack, which was due to the direct exposure of the uncoated sample to SBF. The corrosion products of PLGA/HT-coated sample included HA and $Mg(OH)_2$. The low intensity of $Mg(OH)_2$ in the coated sample confirmed that the presence of a thick PLGA/HT layer can protect the substrate.

3.3. *In vitro* degradation and corrosion

A Mg-based implant should not be degraded before the completion of the healing process; therefore, controlling the corrosion rate would be required for orthopedic applications. Table 3 presents the electrochemical parameters of the uncoated and PLGA/HT composite-coated samples in SBF solution achieved from the polarization test, and Fig. 9 depicts the potentiodynamic polarization curves for the samples. As can be seen, the coated sample presented a corrosion rate different from that of the uncoated sample. The PLGA/HT composite-coated sample had a lower corrosion current density (45.4 $\mu A/cm^2$) than the uncoated sample (243.7 $\mu A/cm^2$). The lower corrosion current density (i_{corr}) can be ascribed to the existence of polymer on the nanocomposite surface that would obstruct the Mg-based active surface at the electrode. Moreover, the PLGA/HT film layer works as one of the anodic barriers and would diminish the solution penetration into the substrate. It also prevents the occurrence of galvanic corrosion. The barrier layer would shift the pitting corrosion potential toward a more positive value, compared to the uncoated sample. Zheludkevich *et al.* [42] reported that the presence of the inorganic ceramic particles enhanced the corrosion protection functions of sol–gel coatings as a result of the respective critical effects of the pore blocking. In the current study, the uncoated and coated nanocomposite specimens were soaked in SBF for 30 min (to obtain the open-circuit potential) prior to the tests to establish uniform corrosion. Over this period, a large volume of corrosion products was formed on the coating layer, which served as an obstacle preventing additional ion release from the substrate and concurrently slowing down the solution infiltration to the substrate, thereby protecting the substrate. The presence of HT particles in the PLGA possibly caused the fast formation of apatite from the Kokubo solution. Due to this precipitation, the PLGA/HT composite coating underwent uniform corrosion. The presence of the HT particles in the PLGA polymer even as agglomerated particles led to the formation of a steady protective layer, which increased the degradation resistance of the Mg-based nanocomposite. Hence, augmenting the degradation resistance of the nanocomposite substrate seems to have a correlation with two major parameters: the barrier effect of the organic–ceramic (PLGA/HT) matrix and the greater sticking strength at the substrate–coating interface due to the chemical bonding between the Mg-based nanocomposite surface and phosphonate groups; both parameters would remarkably decrease the infiltration of the solution into the substrate. The SBF solution ions would enter into the coating layer upon the exposure of the coating to the SBF solution. Such a condition would lead to lower electrochemical corrosion resistance as well as pits formation. Moreover, the dissolution of PLGA/HT as a result of the hydrolysis of the ester links and the generation of acids in the solution would simultaneously cause the production of Ca^{2+} and Zn^{2+} ions from HT in the surrounding media. Because of the greater Ca^{2+} ion concen-

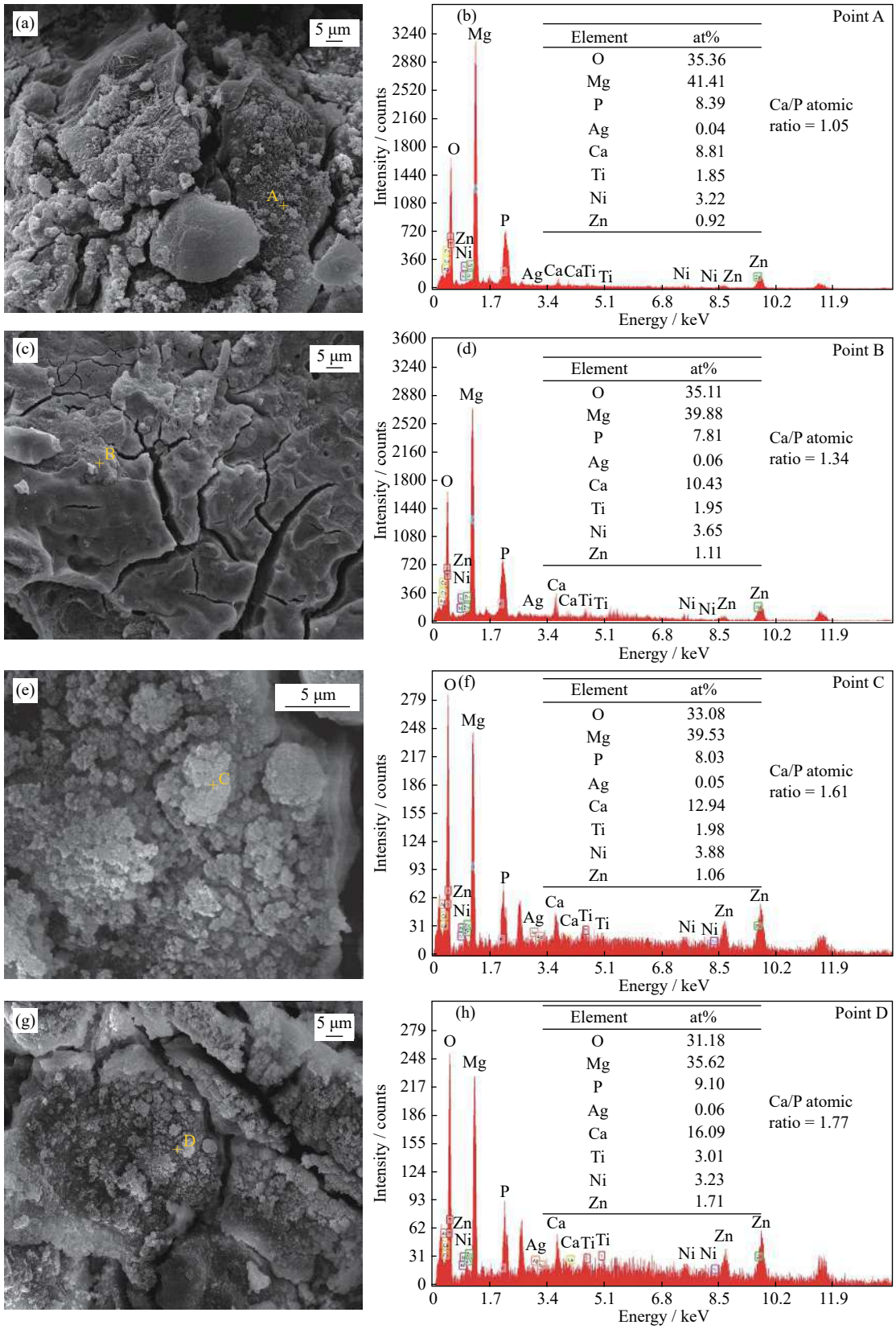

Fig. 7. SEM micrographs and EDS results of (a, b) uncoated and (c, d) 2wt%-, (e, f) 6wt%-, and (g, h) 10wt%-PLGA-coated nanocomposites after immersion in SBF.

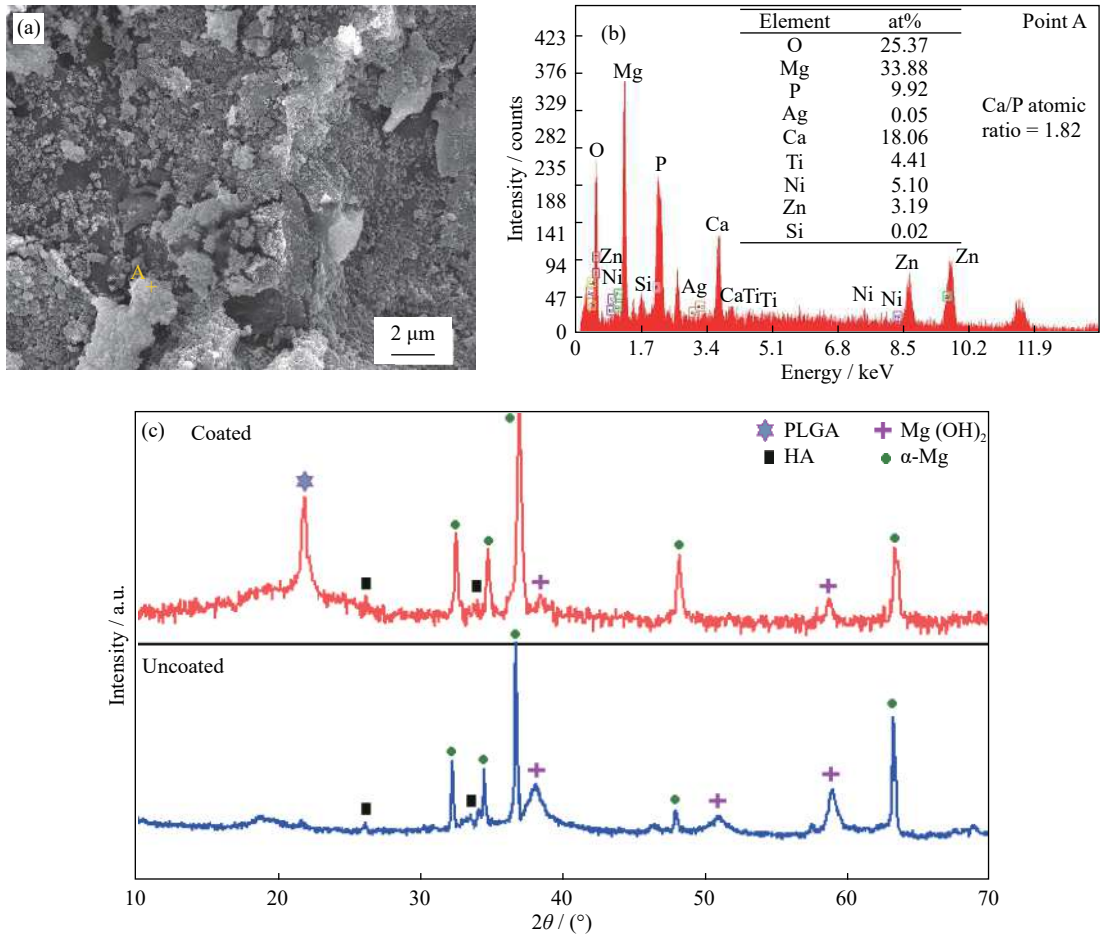

Fig. 8. (a) SEM micrograph of 10wt% PLGA/HT composite-coated sample after immersion in SBF; (b) EDS result for point A in (a); (c) XRD patterns of uncoated and 10wt% PLGA/HT-coated samples after immersion in SBF for 14 d.

Table 3. Electrochemical parameters of the uncoated and PLGA/HT composite-coated specimens in Kokubo solution obtained from the polarization tests

Sample	Corrosion current density, i_{corr} / (μA·cm^{-2})	Corrosion rate, R_{corr} / (mm·a^{-1})
Uncoated	243.7	5.55
PLGA/HT composite coated	45.4	1.03

tration after the HT dissolution in the media, specifically in the solution or at the coating interface, the whole surface of the PLGA base layer would become negatively charged and attract positively charged ions, such as Ca^{2+} and Zn^{2+}, to the interface. Upon the deposition of the positive ions, the whole surface would ultimately become positively charged and lead to the deposition of negatively charged ions, such as OH^-, CO_3^{2-}, and PO_4^{3-}, onto the surface [43]. Finally, the accumulation of the Ca^{2+} and PO_4^{3-} ions as well as the existence of OH^- would lead to the generation of calcium phosphate (apatite) on the specimen surface.

The corrosion current density, i_{corr} (mA/cm^2), was obtained using the following equation: $R_{corr} = 22.85 i_{corr}$ [44]. According to this equation, the corrosion rates (R_{corr}) for the uncoated and coated samples were 5.55 and 1.03 mm/a, respectively.

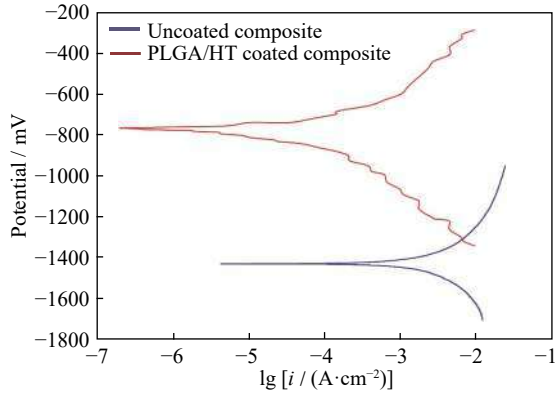

Fig. 9. Potentiodynamic polarization curves of the uncoated and PLGA/HT composite-coated specimens in the SBF solution.

Fig. 10 illustrates the corrosion mechanism of the PLGA/HT composite-coated specimen. The corrosion started with the blistering or bubbling of the coating layer due to

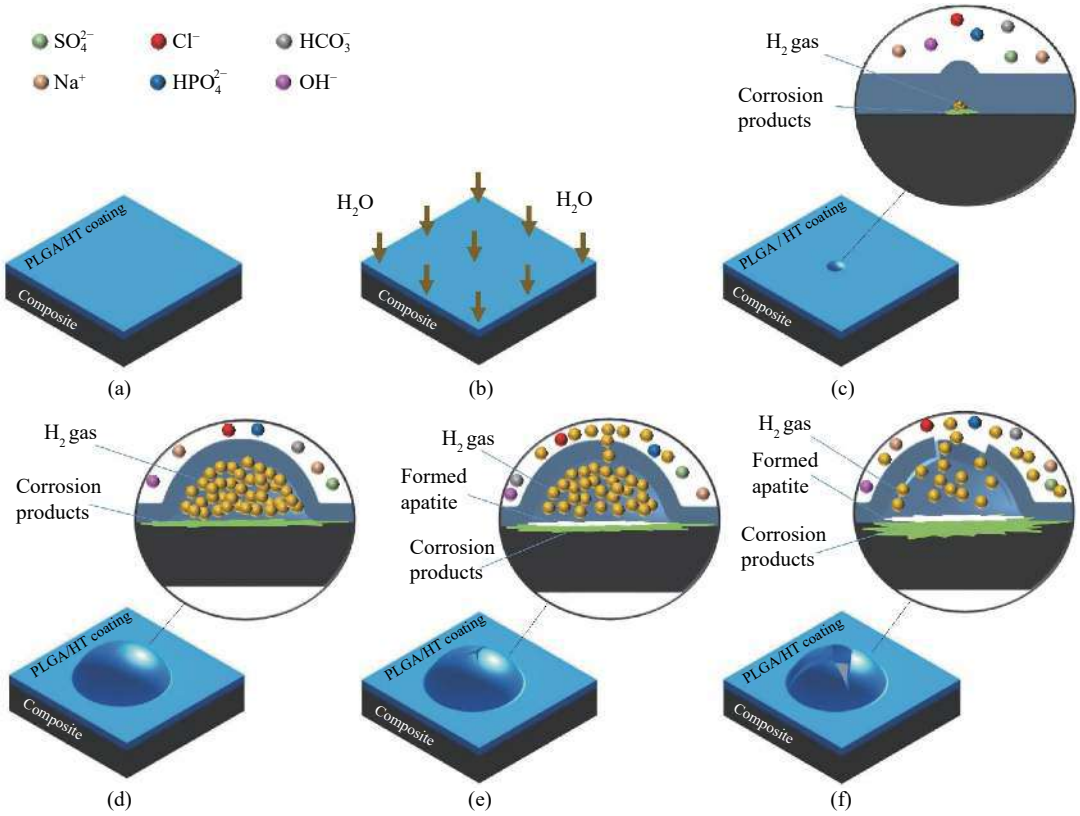

Fig. 10. Schematic illustration of the stages of blistering corrosion mechanism: (a) the initial PLGA/HT composite-coated sample; (b) diffusion of water through the coating; (c) beginning of blistering due to H_2 gas production; (d) blister formation by the H_2 gas accumulation; (e) fracture of the blister due to high pressure of the H_2 gas; (f) increase in corrosion due to the composite exposure.

the Mg-based nanocomposite producing H_2 gas as corrosion product after water infiltration into the coating via osmotic pressure. Fig. 10(c) shows the formed blister at the early stage. Increasing the water absorption and the produced H_2 gas will promote the blister growth. Fig. 10(d) shows the increased volume of the formed blister. After long-term exposure of the specimen to the solution, a crack develops at the top of the blister, exposing the nanocomposite to the solution (Fig. 10(e)). Fig. 10(f) shows the increased corrosion of the composite due to exposure to the solution [45].

The bond strength between the PLGA/HT coating and Mg-based substrate layer was about 6.4 MPa. Due to the poor bonding strength between the coating and substrate layers, further corrosive medium penetrates into the substrate, resulting in the debonding of the coating [46–47]. However, Degner *et al.* [48] showed that despite the poor bonding strength between the coating and substrate, the coating can effectively act as a barrier for the substrate if the coating film thickness is sufficient.

3.4. *In vitro* cytotoxicity

Fig. 11 illustrates the viability of cells cultured on the uncoated Mg-based substrate and PLGA/HT-coated sample extracts for 24 and 48 h. The obtained cell viability values were

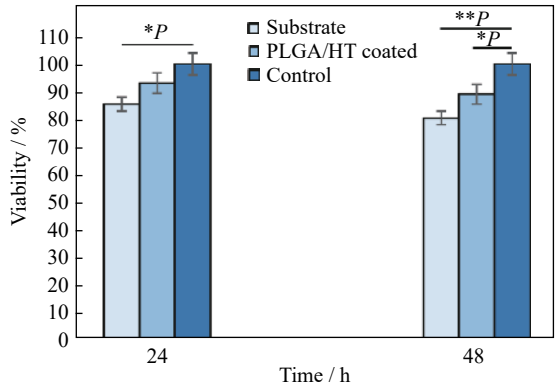

Fig. 11. Viabilities of MG63 osteoblast cells cultured for 24 and 48 h on the uncoated substrate and PLGA/HT coated samples (*P < 0.05; **P < 0.01; Control—Tricalcium phosphate (TCP)).

(80.61 ± 3)% and (89.32 ± 4)% for the substrate and PLGA/HT-coated specimens after 48 h of culture, respectively. The MG63 cells in the PLGA/HT coating extract exhibited better biocompatibility and higher cell viability than those in the substrate. The cytotoxicity of the substrate sample was higher because of the generation of H_2 gas near the implant due to the higher substrate degradation rate and the high cell osmolality caused by a significant difference

between the cell internal and external environments, which results in cell death [49]. Incorporating HT ($Ca_2ZnSi_2O_7$) into the PLGA polymer can provide a constructive environment owing to the rapid deposition of bone-like minerals on the coating layer. The existence of Ca in the HT used in the PLGA-based coating could be a cause of the good cell attachment and the subsequent improvement of bone formation. Similarly, Pant *et al.* [50] showed that the introduction of HA into N6 fibers led to better cell attachment and proliferation compared with the results achieved using plain N6 fibers.

4. Conclusion

This article describes the substantial coating on a Mg-based nanocomposite surface with PLGA/HT through dip coating after the application of mechanical alloying and then sintering to fabricate a Mg–3Zn–0.5Ag–15NiTi nanocomposite substrate. The SEM images of the nanocomposite substrate presented homogenous dispersion of the NiTi NPs in the Mg-based matrix. The coating had a uniform structure with little variations in thickness. The 10wt% PLGA/HT composite coating had a more acceptable barrier impact than the coatings with lower PLGA contents. The Ca/P atomic ratios in the *in vitro* bioactivity assessments after immersion in SBF indicated that the apatite formation amount on the coated specimen was greater than that on the uncoated nanocomposite. Furthermore, the electrochemical tests showed that forming a PLGA/HT layer may efficiently diminish the substrate degradation rate. Incorporating the HT into PLGA increased the bonding strength between the coating and the substrate and the apatite formation on the specimen surface. Finally, our results support the suggestion that utilizing PLGA/HT composite coating on the Mg-based nanocomposite provides the nanocomposite with a high potential for use as implant biomaterial.

Acknowledgement

We wish to thank the support provided by Islamic Azad University of Najafabad, Iran for this research.

References

[1] D.J. Breen and D.J. Stoker, Titanium lines: A manifestation of metallosis and tissue response to titanium alloy megaprostheses at the knee, *Clin. Radiol.*, 47(1993), No. 4, p. 274.

[2] M. Razzaghi, M. Kasiri-Asgarani, H.R. Bakhsheshi-Rad, and H. Ghayour, Microstructure, mechanical properties, and *in-vitro* biocompatibility of nano-NiTi reinforced Mg–3Zn–0.5Ag alloy: Prepared by mechanical alloying for implant applications, *Composites Part B*, 190(2020), art. No. 107947.

[3] M.P. Staiger, A.M. Pietak, J. Huadmai, and G. Dias, Magnesium and its alloys as orthopedic biomaterials: A review, *Biomaterials*, 27(2006), No. 9, p. 1728.

[4] F. Witte, N. Hort, C. Vogt, S. Cohen, K.U. Kainer, R. Willumeit, and F. Feyerabend, Degradable biomaterials based on magnesium corrosion, *Curr. Opin. Solid State Mater. Sci.*, 12(2008), No. 5-6, p. 63.

[5] H.R. Bakhsheshi-Rad, M.H. Idris, M.R. Abdul-Kadir, A. Ourdjini, M. Medraj, M. Daroonparvar, and E. Hamzah, Mechanical and bio-corrosion properties of quaternary Mg–Ca–Mn–Zn alloys compared with binary Mg–Ca alloys, *Mater. Des.*, 53(2014), p. 283.

[6] A.V. Koltygin, V.E. Bazhenov, R.S. Khasenova, A.A. Komissarov, A.I. Bazlov, and V.A. Bautin, Effects of small additions of Zn on the microstructure, mechanical properties and corrosion resistance of WE43B Mg alloys, *Int. J. Miner. Metall. Mater.*, 26(2019), No. 7, p. 858.

[7] Y.Z. Ma, C.L. Yang, Y.J. Liu, F.S. Yuan, S.S. Liang, H.X. Li, and J.S. Zhang, Microstructure, mechanical, and corrosion properties of extruded low-alloyed Mg–*x*Zn–0.2Ca alloys, *Int. J. Miner. Metall. Mater.*, 26(2019), No. 10, p. 1274.

[8] Y. Sun, B.P. Zhang, Y. Wang, L. Geng, and X.H. Jiao, Preparation and characterization of a new biomedical Mg–Zn–Ca alloy, *Mater. Des.*, 34(2012), p. 58.

[9] H.R. Bakhsheshi-Rad, E. Hamzah, M.P. Staiger, G.J. Dias, Z. Hadisi, M. Saheban, and M. Kashefian, Drug release, cytocompatibility, bioactivity, and antibacterial activity of doxycycline loaded Mg–Ca–TiO_2 composite scaffold, *Mater. Des.*, 139(2018), p. 212.

[10] D.R. Monteiro, L.F. Gorup, A.S. Takamiya, A.C. Ruvollo-Filho, E.R. de Camargo, and D.B. Barbosa, The growing importance of materials that prevent microbial adhesion: Antimicrobial effect of medical devices containing silver, *Int. J. Antimicrob. Agents*, 34(2009), No. 2, p. 103.

[11] R. Radha and D. Sreekanth, Insight of magnesium alloys and composites for orthopedic implant applications – A review, *J. Magnesium Alloys*, 5(2017), No. 3, p. 286.

[12] H.X. Li, S.K. Qin, Y.Z. Ma, J. Wang, Y.J. Liu, and J.S. Zhang, Effects of Zn content on the microstructure and the mechanical and corrosion properties of as-cast low-alloyed Mg–Zn–Ca alloys, *Int. J. Miner. Metall. Mater.*, 25(2018), No. 7, p. 800.

[13] A.H.M. Sanchez, B.J.C. Luthringer, F. Feyerabend, and R. Willumeit, Mg and Mg alloys: How comparable are *in vitro* and *in vivo* corrosion rates? A review, *Acta Biomater.*, 13(2015), p. 16.

[14] H. Du, Z.J. Wei, X.W. Liu, and E.L. Zhang, Effects of Zn on the microstructure, mechanical property and bio-corrosion property of Mg–3Ca alloys for biomedical application, *Mater. Chem. Phys.*, 125(2011), No. 3, p. 568.

[15] Y.M. Zhu, A.J. Morton, and J.F. Nie, Improvement in the age-hardening response of Mg–Y–Zn alloys by Ag additions, *Scripta Mater.*, 58(2008), No. 7, p. 525.

[16] Q.D. Wang, J. Chen, Z. Zhao, and S.M. He, Microstructure and super high strength of cast Mg–8.5Gd–2.3Y–1.8Ag–0.4Zr alloy, *Mater. Sci. Eng. A*, 528(2010), No. 1, p. 323.

[17] Ş. Açıkgöz, H. Şevik, and S.C. Kurnaz, Influence of silver addition on the microstructure and mechanical properties of squeeze cast Mg–6Al–1Sn–0.3Mn–0.3Ti, *J. Alloys Compd.*, 509(2011), No. 27, p. 7368.

[18] X.B. Zhang, Z.X. Ba, Z.Z. Wang, X.C. He, C. Shen, and Q. Wang, Influence of silver addition on microstructure and corrosion behavior of Mg–Nd–Zn–Zr alloys for biomedical application, *Mater. Lett.*, 100(2013), p. 188.

[19] M. Mandal, A.P. Moon, G. Deo, C.L. Mendis, and K. Mondal, Corrosion behavior of Mg–2.4Zn alloy micro-alloyed with Ag and Ca, *Corros. Sci.*, 78(2014), p. 172.

[20] M. Razzaghi, M. Kasiri-Asgarani, H.R. Bakhsheshi-Rad, and H. Ghayour, *In vitro* degradation, antibacterial activity and cytotoxicity of Mg–3Zn–*x*Ag nanocomposites synthesized by mechanical alloying for implant applications, *J. Mater. Eng. Perform.*, 28(2019), No. 3, p. 1441.

[21] V. Kavimani, K.S. Prakash, and T. Thankachan, Experimental investigations on wear and friction behavior of SiC@r-GO reinforced Mg matrix composites produced through solvent-based powder metallurgy, *Composites Part B*, 162(2019), p. 508.

[22] S. Wakeel, V. Manakari, G. Parande, M.S. Kujur, A.A. Khan, and M. Gupta, Synthesis and mechanical response of NiTi SMA nanoparticle reinforced Mg composites synthesized through microwave sintering process, *Mater. Today*: *Proc.*, 5(2018), No. 14, p. 28203.

[23] Y.F. Zheng, X.N. Gu, Y.L. Xi, and D.L. Chai, *In vitro* degradation and cytotoxicity of Mg/Ca composites produced by powder metallurgy, *Acta Biomater.*, 6(2010), No. 5, p. 1783.

[24] Z. Esen, TiNi reinforced magnesium composites by powder metallurgy, [in] W.H. Sillekens, S.R. Agnew, N.R. Neelameggham, S.N. Mathaudhu, eds., *Magnesium Technology 2011*, Springer, Cham, Switzerland, 2011, p. 457.

[25] W. Guo, H. Kato, S.L. Lü, and S.S. Wu, Porous NiTi particle dispersed Mg–Zn–Ca bulk metallic glass matrix composites, *Materials*, 11(2018), No. 10, p. 1959.

[26] Z. Esen, The effect of processing routes on the structure and properties of magnesium–TiNi composites, *Mater. Sci. Eng. A*, 558(2012), p. 632.

[27] Y. Wang, Z.H. Wu, H. Zhou, Z.D. Liao, and H.F. Zhang, Corrosion properties in a simulated body fluid of Mg/β-TCP composites prepared by powder metallurgy, *Int. J. Miner. Metall. Mater.*, 19(2012), No. 11, p. 1040.

[28] M.D. Pereda, C. Alonso, L. Burgos-Asperilla, J.A. del Valle, O.A. Ruano, P. Perez, and M.A.F.L. de Mele, Corrosion inhibition of powder metallurgy Mg by fluoride treatments, *Acta Biomater.*, 6(2010), No. 5, p. 1772.

[29] M.K. Datta, D.-T. Chou, D. Hong, P. Saha, S.J. Chung, B. Lee, A. Sirinterlikci, M. Ramanathan, A. Roy, and P.N. Kumta, Structure and thermal stability of biodegradable Mg–Zn–Ca based amorphous alloys synthesized by mechanical alloying, *Mater. Sci. Eng. B*, 176(2011), No. 20, p. 1637.

[30] Y.H. Gao, A. Yerokhin, and A. Matthews, Deposition and evaluation of duplex hydroxyapatite and plasma electrolytic oxidation coatings on magnesium, *Surf. Coat. Technol.*, 269(2015), p. 170.

[31] N. Li and Y.F. Zheng, Novel magnesium alloys developed for biomedical application: A review, *J. Mater. Sci. Technol.*, 29(2013), No. 6, p. 489.

[32] H.R. Bakhsheshi-Rad, E. Hamzah, M. Daroonparvar, M.A.M. Yajid, and M. Medraj, Fabrication and corrosion behavior of Si/HA nano-composite coatings on biodegradable Mg–Zn–Mn–Ca alloy, *Surf. Coat. Technol.*, 258(2014), p. 1090.

[33] H.R. Bakhsheshi-Rad, E. Hamzah, A.F. Ismail, M. Aziz, M. Kasiri-Asgarani, H. Ghayour, M. Razzaghi, and Z. Hadisi, *In vitro* corrosion behavior, bioactivity, and antibacterial performance of the silver-doped zinc oxide coating on magnesium alloy, *Mater. Corros.*, 68(2017), No. 11, p. 1228.

[34] E.V. Parfenov, A. Yerokhin, R.R. Nevyantseva, M.V. Gorbatkov, C.-J. Liang, and A. Matthews, Towards smart electrolytic plasma technologies: An overview of methodological approaches to process modelling, *Surf. Coat. Technol.*, 269(2015), p. 2.

[35] T. Hanas, T.S.S. Kumar, G. Perumal, and M. Doble, Tailoring degradation of AZ31 alloy by surface pre-treatment and electrospun PCL fibrous coating, *Mater. Sci. Eng. C*, 65(2016), p. 43.

[36] G.X. Liang and R. Schulz, Synthesis of binary Mg-based alloys by mechanical alloying, *J. Metastable Nanocryst. Mater.*, 12(2002), p. 93.

[37] E.M. Salleh, S. Ramakrishnan, and Z. Hussain, Synthesis of biodegradable Mg–Zn alloy by mechanical alloying: Effect of milling time, *Procedia Chem.*, 19(2016), p. 525.

[38] D.R. Askeland, P.P. Phulé, W.J. Wright, and D.K. Bhattacharya, The Science and Engineering of Materials, Springer, Dordrecht, 2003.

[39] ASTM International, ASTM G59-97: *Standard Test Method for Conducting Potentiodynamic Polarization Resistance Measurements*, ASTM International, West Conshohocken, 2009.

[40] H.R. Bakhsheshi-Rad, M. Akbari, A.F. Ismail, M. Aziz, Z. Hadisi, E. Pagan, M. Daroonparvar, and X.B. Chen, Coating biodegradable magnesium alloys with electrospun poly-L-lactic acid-åkermanite-doxycycline nanofibers for enhanced biocompatibility, antibacterial activity, and corrosion resistance, *Surf. Coat. Technol.*, 377(2019), art. No. 124898.

[41] L. Yang and E.L. Zhang, Biocorrosion behavior of magnesium alloy in different simulated fluids for biomedical application, *Mater. Sci. Eng. C*, 29(2009), No. 5, p. 1691.

[42] M.L. Zheludkevich, R. Serra, M.F. Montemor, I.M.M. Salvado, and M.G.S. Ferreira, Corrosion protective properties of nanostructured sol–gel hybrid coatings to AA2024-T3, *Surf. Coat. Technol.*, 200(2006), No. 9, p. 3084.

[43] M. Diba, O.-M. Goudouri, F. Tapia, and A.R. Boccaccini, Magnesium-containing bioactive polycrystalline silicate-based ceramics and glass-ceramics for biomedical applications, *Curr. Opin. Solid State Mater. Sci.*, 18(2014), No. 3, p. 147.

[44] Z.M. Shi, M. Liu, and A. Atrens, Measurement of the corrosion rate of magnesium alloys using Tafel extrapolation, *Corros. Sci.*, 52(2010), No. 2, p. 579.

[45] B.S. Liu, Y.F. Kuang, Y.S. Chai, D.Q. Fang, M.G. Zhang, and Y.H. Wei, Degradation research of protective coating on AZ91D Mg alloy components via simulated contamination, *J. Magnesium Alloys*, 4(2016), No. 3, p. 220.

[46] H.R. Bakhsheshi-Rad, E. Hamzah, A.F. Ismail, Z. Sharer, M.R. Abdul-Kadir, M. Daroonparvar, S.N. Saud, and M. Medraj, Synthesis and corrosion behavior of a hybrid bioceramic–biopolymer coating on biodegradable Mg alloy for orthopedic implants, *J. Alloys Compd.*, 648(2015), p. 1067.

[47] H.R. Bakhsheshi-Rad, E. Hamzah, A.F. Ismail, M. Daroonparvar, M. Kasiri-Asgarani, S. Jabbarzare, and M. Medraj, Microstructural, mechanical properties and corrosion behavior of plasma sprayed NiCrAlY/nano-YSZ duplex coating on Mg–1.2Ca–3Zn alloy, *Ceram. Int.*, 41(2015), No. 10, p. 15272.

[48] J. Degner, F. Singer, L. Cordero, A.R. Boccaccini, and S. Virtanen, Electrochemical investigations of magnesium in DMEM with biodegradable polycaprolactone coating as corrosion barrier, *Appl. Surf. Sci.*, 282(2013), p. 264.

[49] H.R. Bakhsheshi-Rad, X.B. Chen, A.F. Ismail, M. Aziz, E. Abdolahi, and F. Mahmoodiyan, Improved antibacterial properties of an Mg–Zn–Ca alloy coated with chitosan nanofibers incorporating silver sulfadiazine multiwall carbon nanotubes for bone implants, *Polym. Adv. Technol.*, 30(2019), No. 5, p. 1333.

[50] H.R. Pant, P. Risal, C.H. Park, L.D. Tijing, Y.J. Jeong, and C.S. Kim, Core–shell structured electrospun biomimetic composite nanofibers of calcium lactate/nylon-6 for tissue engineering, *Chem. Eng. J.*, 221(2013), p. 90.